Journal of Molecular Structure 1171 (2018) 682–695

Contents lists available at ScienceDirect

Journal of Molecular Structure

journal homepage: http://www.elsevier.com/locate/molstruc

Structural, vibrational, UV–vis, quantum-chemical properties, molecular docking and anti-cancer activity study of annomontine and *N*-hydroxyannomontine β-carboline alkaloids: A combined experimental and DFT approach

Renyer A. Costa [a, *], Earle Silva A. Junior [b], Guilherme Braule P. Lopes [a], Maria Lucia B. Pinheiro [a], Emmanoel V. Costa [a], Daniel P. Bezerra [c], Kelson Oliveira [a, **]

[a] Department of Chemistry, Federal University of Amazonas (DQ-UFAM), 69077-000 Manaus, AM, Brazil
[b] Federal Institute of Science and Technology of Amazonas (IFAM), 69020-120 Manaus, AM, Brazil
[c] Gonçalo Moniz Institute, Oswaldo Cruz Fundation (IGM/FIOCRUZ-BA), Salvador, Bahia, Brazil

ARTICLE INFO

Article history:
Received 8 February 2018
Received in revised form
9 June 2018
Accepted 11 June 2018
Available online 14 June 2018

Keywords:
Annomontine
N-hydroxyannomontine
UV–Vis
DFT
Molecular docking
Anti-cancer

ABSTRACT

A theoretical and experimental DFT study of the vibrational, structural and quantum properties of annomontine (**1**) and *N*-hydroxyannomontine (**2**) alkaloids using the B3LYP exchange-correlation functional with 6-311G (2d, p) basis set is presented. The theoretical geometry optimization data of the two structures were compared with the X-ray data of (1) in the associated literature and a conformational study is presented for both molecules, providing a good comprehension of the conformational stability. In addition, natural bond orbitals (NBOs), HOMO-LUMO energy gap and mapped molecular electrostatic potential surface (MEPS) calculations were also performed at the same calculation approach. The calculated UV spectra agreed well with the measured experimental data, with transitions assigned. The comparative IR studies confirmed the intramolecular hydrogen bonds of the conformations and the intermolecular hydrogen bonds of dimeric forms and also revealed several characteristic vibrations for the structures. Molecular docking studies with DNA Topoisomerase II-DNA complex showed binding free energies of −11.5 and −10.6 kcal/mol for **2** and **1** respectively, while for amsacrine, used for the treatment of leukemia, and doxorubicin, used for the treatment of breast cancer, bladder cancer, Kaposi's sarcoma, and acute lymphocytic leukemia, the presented binding free energies values are −10.0 and −9.9 kcal/mol respectively, revealing good bind affinities of the tested alkaloids with the complex. In vitro cytotoxicity assay revealed an expressive antitumor activity of *N*-hydroxyannomontine against human hepatocellular carcinoma cell line HepG2.

1. Introduction

The β-carboline alkaloids are a large group of natural and synthetic indole alkaloids that possess a common tricyclic pyrido [1,2] indole ring structure [3] which are widely distributed in nature, including various plants, foodstuffs, marine creatures, insects, mammalians as well as human tissues and body fluids. These compounds are of great interest due to their diverse biological activities deserving attention the effects on the central nervous system (CNS), such as their affinity with benzodiazepine receptors (BZRs), 5-HT_{2A} and 5-HT_{2C} receptors [4,5] and their potent antitumor [6–8], antiviral [9,10] antimicrobial [11] and antiparasitic activities [12,13].

The β-carboline alkaloids can be categorized according to the saturation of their N-containing six-membered ring. Unsaturated members are named as fully aromatic β-carbolines (βCs), whereas the partially or completely saturated ones are known as dihydro-β-carbolines (βDHCs) and tetrahydro-β-carbolines (THβCs), respectively [14]. In the βCs group the pyramidine-β-carboline type alkaloids are a very rare class of compounds that has only three members and whose structures are characterized by a 2-

* Corresponding author.,
** Corresponding author.
E-mail addresses: renyer.costa@gmail.com (R.A. Costa), kelsonmota@ufam.edu.br (K. Oliveira).

https://doi.org/10.1016/j.molstruc.2018.06.054
0022-2860/

aminopyramidine unit linked to a harman moiety, being interesting from both structural and biological points of view. The first two members of this class, annomontine (**1**) and methoxyannomontine (**2**) were described for the first time in 1982 as natural metabolite from *Annona montana* [15] and after from *Annona reticulata* L., *Neolitsea konishii* and by synthesis [16–18]. The third member, *N*-hydroxyannomontine (3) was isolated only once (together with 1) by one of the co-authors from *Annona foetida* in 2006 with NMR chemical shifts completely assigned [19,20]. However, combined theoretical and experimental investigations of their conformational, reactive, spectroscopic and quantum properties and molecular docking studies still lack in the literature. Also the determination of the vibrational frequencies and electronic transitions of the UV bands has not been investigated yet for these pyramidine-β-carboline alkaloids.

From this premise this work discusses annomontine (**1**) and *N*-hydroxyannomontine (**2**) (obtained from *Annona foetida*) from a theoretical view (geometry optimization, NBO and MEPS calculations) based on experimental data (NMR, UV, FTIR), providing a more complete description of their structures and spectral behavior. To the best of our knowledge no theoretical molecular modeling study that discusses the bond lengths, planar and dihedral angles, HOMO-LUMO energies and MEPS was previously presented and a detailed description of the spectroscopic behavior of the title compounds with the help of quantum chemical DFT calculations, along with NBO calculations, has not been performed yet. The pharmacological and biochemical properties of these two alkaloids are scarcely documented and, in view of the antineoplastic potential registered in the PASS (prediction of activity spectra), molecular docking calculations with DNA topoisomerase II-DNA complex and cytotoxic assays *in vitro,* with both structures, were performed with the aim of contributing for the knowledge of the biological activity of these kind of molecules.

2. Methodologies

2.1. Computacional methods

The compounds annomontine (**1**) and *N*-hydroxyannomontine (**2**) were isolated from *Annona foetida* and the experimental spectroscopy data obtainment (FT-IR, UV–Vis) and the isolation methodology were previously reported [19,20]. The theoretical quantum chemical calculations were performed using the Gaussian 09 Program (Revision D.01) [21] on the Debian LINUX (5.0 version) platform on an INTEL CORE™ i7 PC with 16 GB RAM. The DFT approach was used to optimize the geometry using the 6-311G (2d,p) basis sets and the B3LYP functional. Potential energy surfaces were scanned for the structures using relaxed dihedral angle scan coordinates (the calculation consisted in 60 steps varying by 6°, totalizing a 360° turn, the dihedral angle between the C5′ and N2 atoms) and all minima geometries were fully optimized by the force gradient method, using Berny's algorithm and standard analytical harmonic vibrational analysis (no imaginary frequencies or negative eigenvalues were found). The theoretical IR spectra were obtained from the DFT intensities in combination with the calculated vibrational wavenumbers uniformly scaled by factor of 0.98 (no imaginary frequencies or negative eigenvalues were found). The UV spectra were calculated using the TD-B3LYP-FC functional with 6-311G (2d,p) basis set in methanol using PCM model. The NBO values were obtained with NBO 3.1 program, as implemented in the GAUSSIAN 09 package using the same theory level. The assignments of the calculated IR wavenumbers are aided by the animation option of GAUSSVIEW 5.0 program, which gives a visual presentation of the vibrational modes [22]. The potential energy distribution (PED) was calculated with the help of VEDA4 software package [23].

2.2. Cytotoxicity assay

HepG2 (human hepatocellular carcinoma), HL-60 (human promyelocytic leukemia), K-562 (human chronic myelogenous leukemia) and B16–F10 (murine melanoma) tumor cell lines were obtained from the American Type Culture Collection (ATCC, Manassas, VA, USA). Cells were cultured in complete medium with appropriate supplements as recommended by ATCC. All cell lines were tested for mycoplasma using a mycoplasma stain kit (Sigma-Aldrich) to validate the use of cells free from contamination. Primary cell culture of peripheral blood mononuclear cells (PBMC) was obtained by standard ficoll density protocol. The Research Ethics Committee of the Oswaldo Cruz Foundation (Salvador, Bahia, Brazil) approved the experimental protocol (# 031019/2013). To evaluate the cytotoxicity of the compounds, the alamar blue assay was performed after 72 h of exposure to the compounds [24,25]. After 24 h of incubation, the compounds dissolved in DMSO were added to each well and incubated for 72 h. Doxorubicin was used as positive control. The negative control received the same amount of DMSO. Four hours before the end of the incubation period, 20 μL of stock solution (0.312 mg/mL) of alamar blue were added to each well. The absorbances were measured at wavelengths of 570 nm and 595 nm using a plate reader (SpectraMax® plus 384). The half maximal inhibitory concentration IC_{50} was determined from non-linear regression using the GraphPad Prism Software version 5.0.

3. Results and discussion

3.1. Geometry parameters and conformational analysis molecular electrostatic maps

The theoretical geometry optimization results of the studied molecules, which were calculated at B3LYP/6-311G (2d, p) approach (Fig. 1), were compared with X-ray data for (**1**) presented in the literature [26] (see Table S1). Both molecules (strucutures 1 and 2) showed C1 symmetry, with the most stable conformations showing energy electronic values of −852.253067 and −927.43589 a.u. respectively. The RMSD (Root Mean Square Deviation) are 0.0153 and 0.0130 for (**1**) and (**2**) respectively in respect to the interatomic distances, and 0.9158 and 0.9765 respectively for the torsion angles. These values reveal the accuracy of the theoretical calculations, making them reliable for the discussion of the molecular geometry and conformations -of the title molecules.

For structure (**1**) the bond lengths values revealed that A ring presents a certain uniformity (~1.39 Å) except for C5a-C8a bond (1.42 Å), B ring shows non uniformity, with distinct values for all bonds, 1.45 (C5a-C4a), 1.42 (C4a-C1a), 1.37 (C1a-N9), 1.38 (N9–C8a) and 1.42 (C8a-C5a), while the experimental data are 1.44, 1.43, 1.37, 1.38 and 1.41 Å respectively. In C ring the C=C bonds showed certain uniformity (~1.39 Å) except the *C*–N bonds (C3–N2 and C1–N2) that presented bond lengths of ~1.33 Å in conformity with experimental data too. Concerning to the bond angles the entire structure presented distortions in all rings. A ring showed values of 120.70° (C7–C6–C5), 119.03° (C6–C5–C5a), 119.54° (C5–C5a-C8a), 121.54° (C5a-C8a-C8) and 117.67° (C8a-C8-C7) (RMSD = 1.29 with experimental data), B ring showed distinct angles values revealing a certain non uniformity and the RMSD with experimental data is 0.88. C ring presented similar bond angles values (~119°) except for C4–C3–N2 (124.2°) and for C4a-C4-C3 (117.74°) (RMSD with experimental data is 0.84) and D ring showed distinct values for all angles with a RMSD with experimental data of 0.77. All bond angles and lengths are summarized in table S1. Potential energy surfaces

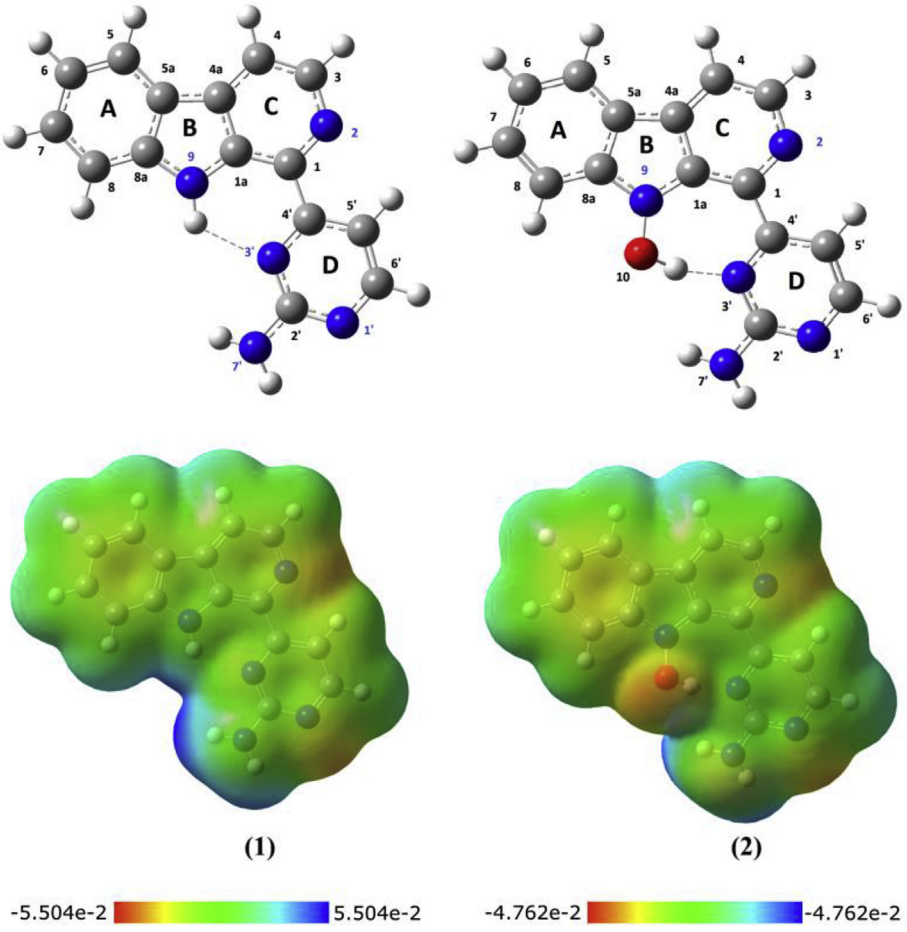

Fig. 1. Optimized structures and MEPS of annomontine **(1)** and N-hydroxyannomontine **(2)**.

scan calculations (Fig. 2) reveals that conformation 1A presents the lowest electronic energy followed by conformations 1C (1A→1C 10 kcal/mol), 1E (1A→1E 10.5 kcal/mol), 1B (1A→1B 11 kcal/mol), 1F (1A→1F 11.1 kcal/mol) and 1D (presented the highest energy, 1A→1D 14 kcal/mol). Conformation 1A presents a *quasi* planar structure presenting a dihedral angle (C1a-C1-C4′-C3′) value of 5.009° (while the X-ray analysis showed a dihedral angle of 5.60°), and a hydrogen bond between H9 and N3′ atoms (bond length of 2.16 Å) that promotes high stability to this conformation. Conformations 1B and 1F present an angle of ~90° between C and D rings which promotes a steric repulsion between the π clouds of C ring and the H5′ atom and N3′ lone pairs. Conformer 1D presents a planar structure however the steric repulsions between H9 and H5′ atoms promotes instability to this stage. Conformations 1C and 1E present a dihedral angle (C1a–C1–C4′–N3′) of 140.0° and −139.99° respectively being the most stable structures after A

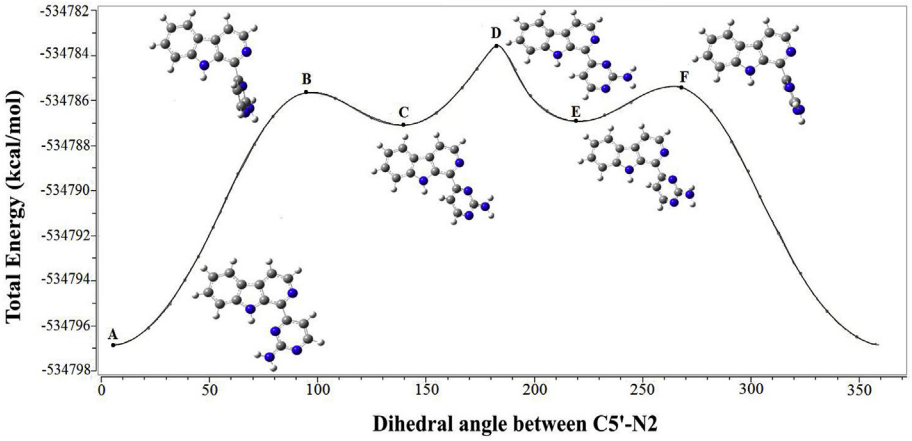

Fig. 2. Potential energy scan calculations for structure (1).

due to the minimization of the steric repulsions between the π clouds of C ring and the H5′ atom and N3′ lone pairs. The calculated energetic barriers for the rotations are 11 kcal/mol (1A→1C) and 4 kcal/mol (1C→1E).

For structure **(2)** (see Fig. 1 and Table S1) the bond lengths values revealed that A ring presents a certain uniformity (~1.39 Å) except for C5a–C8a bond (1.41 Å). The B and C rings presents different values for all, 1.41 Å (C8a–C5a), 1.44 Å (C5a–C4a), 1.37 Å (C1a–N9), 1.39 Å (C3–C4), 1.33 Å (C3–N2), 1.34 Å (N2–C1), 1.41 Å (C1–C1a) and 1.43 Å (C4a–C1a). In D ring the C=C bonds showed certain uniformity (~1.39 Å) and the *C*–N bonds presented variations 1.34 Å (N1′–C2′), 1.34 Å (C2′–N3′ and N3′–C4′) and 1.37 Å (C2′–N7′). The distortions presented in the rings B, C and D are due to de presence of hydroxyl group that forms a seven membered ring (H–O10–N9–C1a–C1–C4′–N3′) promoting a non uniformity and a non planarity for the structure, which shows a dihedral angle (C1a–C1–C4′–N3′) of 11.72°. Concerning to the bond angles the entire structure showed distortions, A ring presents distinct values for all angles, B ring shows certain uniformity in its angles (~107°), except for C8a–N9–C1a (110.7°) and C8a–C5a–C4a (106.33°) bonds, C ring like ring A presents distortions in all angles, with values of 117.54° (C4a–C4–C3), 123.63°(C4–C3–N2), 119.37°(N2–C1–C1a), 119.39°(C1–C1a–C4a) and 118.73° (C1a–C4a–C4). D ring presents bond angles values similar to **(1)**. Potential energy surfaces scan calculations (Fig. 3) revealed that conformation 2D presents de highest energy value being the most instable stage due to the steric repulsion between OH group and H5′ atom. Conformation 2D is followed by conformations 2F (−927.41490 a.u.), 2C (−927.41524 a.u.), 2B (−927.41579 a.u.), 2H (−927.41611 a.u.), 2E (−927.41684 a.u.), 2G (−927.41782 a.u.) and 2A (−927.4358 a.u., most stable conformation). Conformations 2B and 2F like in structure 1 presents an angle of ~90° between C and D rings planes, which promotes a steric repulsion between the π clouds of C ring and the H5′ atom and N3′ lone pairs, and a steric repulsion between the π clouds of D ring and the lone pairs of O10 atom, promoting certain instability. Conformation 2C presents a dihedral angle of 125, 07° between the N2 and C5′ atoms and can be classified as a transition conformational structure between the 2B and 2D conformations. This conformation has less energy than the conformation 2Dbecause the nitrogen atoms N2 and N3′ have a distance of 2.906 Å, while in conformation 2D this distance is 2.617 Å, increasing the repulsion of the lone pairs. Conformation 2E resembles 2C conformation but the N3′ atom is directed over the *C*-ring, while in 2C conformation N3′ atom is directed under the *C*-ring. Conformation 2E presents a distance of 2.906 Å between the N2 and N3′ atoms and the dihedral angle between the N2 and C5′ is −126.08°, in others words, conformation 2E constitutes a 60° rotation around the C1–C4′ bonds axis starting from the conformation 2C. Conformation 2G, a potential energy well between conformations 2F and 2H, presents a dihedral angle of −31.32° between the N2 and C5′ atoms, which promotes certain stability. This conformation presents a distance of 3.52 Å between the N2 and N3′ atoms, providing less repulsion between the nitrogen lone pairs, thus giving for this conformation a certain stability in relation to the conformations 2B, 2C, 2D, 2E, 2F and 2H. However the distance between N3′- O10 (2.82 Å) and N2 – H5' (2.59 Å) atoms gives to the structure a higher total energy value in relation to conformation 2A. Conformation 2A presents the lowest electronic total energy due to the hydrogen bond between H10 and N3' (bond length of 1.63 Å) atoms, which promotes high stability to this stage. The calculated energetic barriers for the rotations are 13 kcal/mol (2A →2C), 6 kcal/mol (2C→2E), 5 kcal/mol (2E→2G) and 4.5 kcal/mol (2G→2A).

3.2. Electrostatic potential maps

The Molecular Electrostatic Potential Surface (MEPS) is a plot of electrostatic potential mapped onto the constant electron density surface. The MEPS has been used primarily for predicting sites and relative reactivity towards electrophilic attack, in studies of biological recognition and hydrogen bonding interactions. The negative electrostatic potential corresponds to an attraction of the proton by the concentrated electron density in the molecule (and is colored in shades of red), the positive electrostatic potential corresponds to repulsion of the proton by atomic nuclei in regions where low electron density exists and the nuclear charge is incompletely shielded (and is colored in shades of blue). Potential increases in the order red < yellow < green < blue. The molecular electrostatic potential map surface (MEPS) (Fig. 1) for structure **(1)** showed polarized regions with positive potentials over H7' (0.053 a.u. and 0.043 a.u.), H9 (0.046 a.u.), H8 (0.026 a.u.), H4 (0.019 a.u.) and H5 (0.019 a.u.) atoms and negative potentials over A ring (−0.0208 a.u.), B ring (−0.011 a.u.), C ring (−0.016 a.u.), D ring (−0.011 a.u.), over N2 (−0.033 a.u.) and N1' (−0.036 a.u.) atoms, leading to infer that the lone pair of these N atoms are not incorporated into the aromatic π system. N3′ has a potential less negative (−0.0136 a.u.) in relation to the other nitrogens due to the charge transfer involved in the hydrogen bond N9–H9···N3′. N9

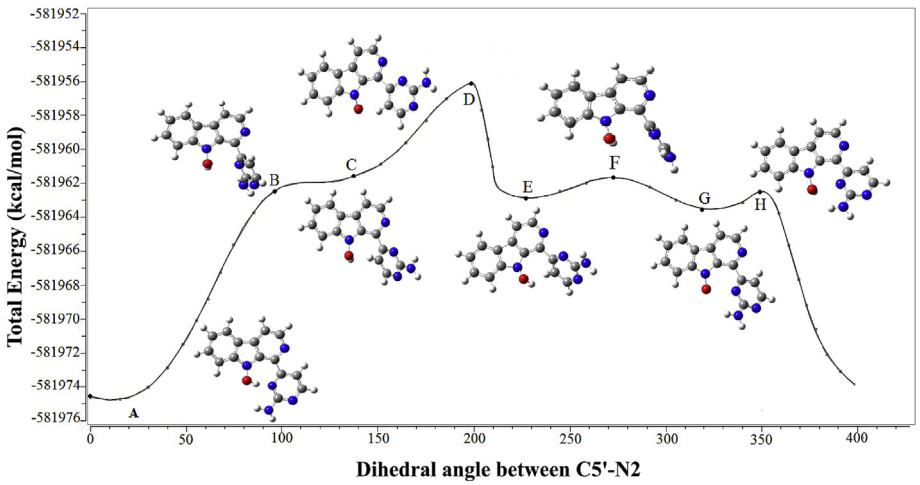

Fig. 3. Potential energy scan calculations for structure (2).

and N7′ atoms presents green surface, indicating that the electron pairs are incorporated in the aromatic system. Based on the opposite charges, two dimers were proposed (Fig. 4), presenting the intermolecular hydrogen bonds N7′—H···N1′ and N7′—H···N3′ for dimer I, and N7′—H···N2 bond for dimer II. Concerning the stability of the proposed dimers in relation to the monomer of structure **(1)**, the analysis was given through the values of ΔE (interaction energy), defined as follows:

$$\Delta E = E_{\text{Dimer}} - 2E_{\text{Monomer}}$$

The dimer I showed Δ*E* value of −9.2 kcal/mol, while for the dimer II, the calculated Δ*E* revealed a value of −6.66 kcal/mol, indicanting stabilization of the proposed dimers. Relative to the bond lenghts of the intermolecular N7′—H···N1′ and N7′—H···N3′ hydrogen bonds of dimer I, the calculated distances are equal to 2.079 and 2.185 Å respectively. For dimer II the length of the intermolecular hydrogen bond N7′—H···N2 is equal to 2.116 Å. For structure **(2)** the MEPS (Fig. 1) showed polarized regions with positive potentials over H7' (0.047 and 0.041 a.u.), H5 (0.020 a.u.), H5 (0.020 a.u.), H4 (0.022 a.u.) and H5' (0.018 a.u.) atoms, and

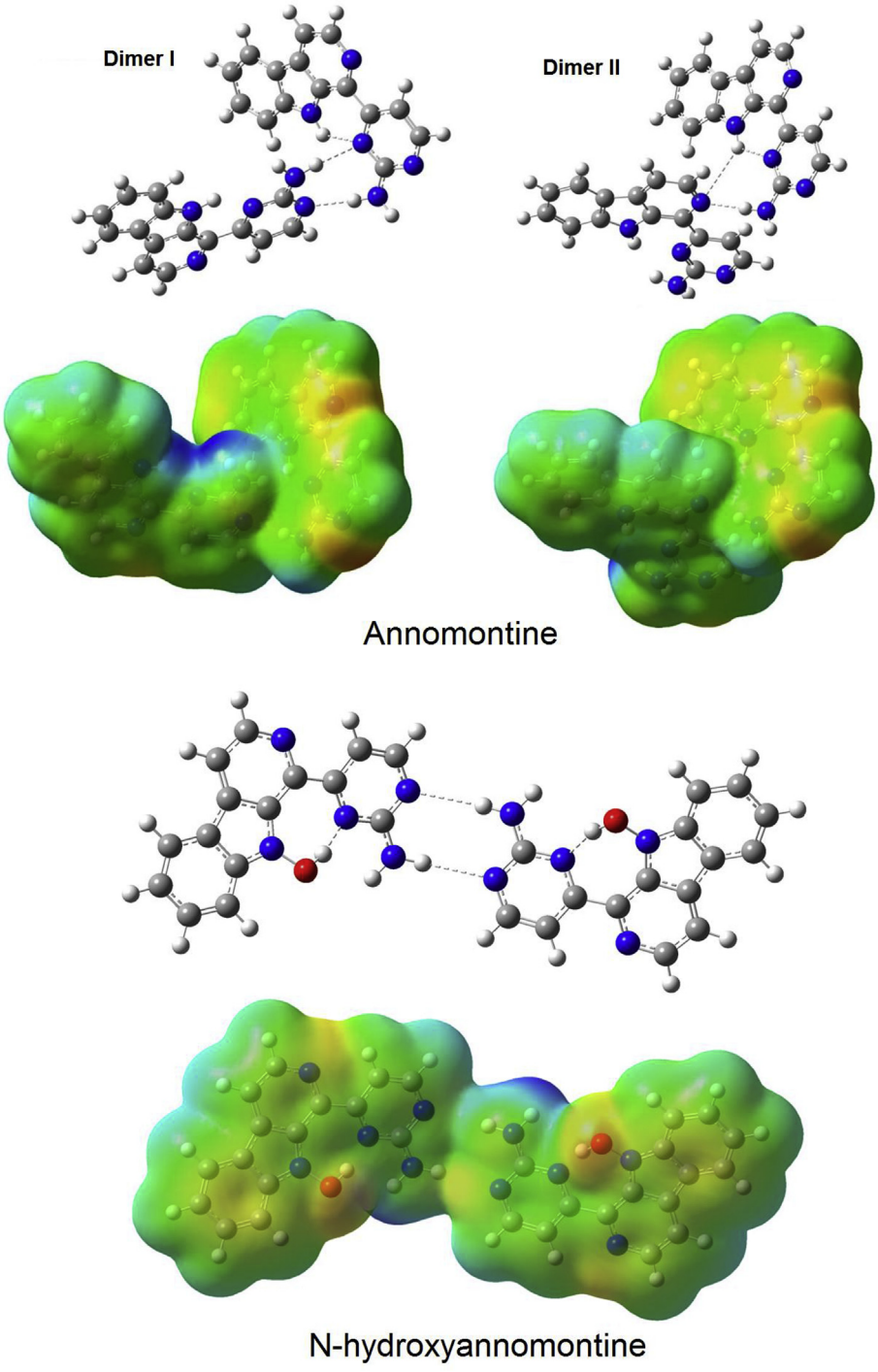

Fig. 4. Proposed dimers for structures (**1**) and (**2**), featuring hydrogen bonds (dashed line) and MEPS (molecular electrostatic potential surfaces).

negative potentials over O10 (−0.035 a.u.), N2 (−0.027 a.u.), N1' (−0.031 a.u.) and N7' (−0.018 a.u.) atoms and over A ring (−0.023 a.u.), B ring (−0.01 a.u.), C ring (−0.013 a.u.) and D ring (−0.005 a.u.). Likewise structure **(1)**, N2 and N1′ atoms are not incorporated into the aromatic π system and N9 atom presents green surface, indicating that the electron pair is incorporated in the aromatic system. For N7′ atom this is not verified. N3′ has a potential much less negative than the calculated for alkaloid (1) (−0.0079 a.u.), due to the charge transfer involved in the hydrogen bond O10—H···N3′ be more effective. Based on the opposite charges, a dimer was proposed for alkaloid **(2),** see Fig. 4. Concerning to the stability of the proposed dimer for structure (2), the analysis through the values of interaction energy ΔE (as mentioned above), revealed that the proposed dimer is more stable than the isolated monomer, revealing a $\Delta E = -2.56$ kcal/mol. Relative to the bond lenghts of the two intermolecular (N7′—H···N1′) hydrogen bonds presented in the proposed dimer, the calculated distances are equal to 2.920 and 2.899 Å respectively.

3.3. HOMO and LUMO analysis

The energy gap between the HOMO (Highest Occupied Molecular Orbital) and LUMO (Lowest Unoccupied Molecular Orbital) is very important for determining the electrical properties, kinetic stability, optical polarizability and chemical reactivity descriptors, such as hardness and softness, of a molecule. The concept of hardness (η) is related to a compound's reactivity and is a property that measures the extent of chemical reactivity to which the addition of a charge stabilizes the system. The chemical potential (μ) provides a global reactivity index and is related to charge transfer from a system of higher chemical potential to one of lower chemical potential. Electronegativity (χ) is the power to attract electrons which is equal to the negative of the chemical potential. All these properties are defined as follows [27,28]:

$$\eta = \frac{(I - A)}{2}$$

$$\mu = \frac{-(I + A)}{2} = -\chi$$

where A is the electron affinity and I is the ionization potential of the molecule. The ionization energy and electron affinity are obtained from the HOMO and LUMO energies as $I = -E_{HOMO}$ and $A = -E_{LUMO}$. In terms of chemical hardness, a large HOMO-LUMO gap indicates a hard molecule and is related to more stable molecules, whereas a small gap indicates a soft molecule and is related to a more reactive molecule.

Another important descriptor is the electrophilicity index (ω), a global reactivity index that is related to chemical hardness and chemical potential. The electrophilicity index measures the global electrophilic nature of a molecule and was proposed by Parr et al. [29] as a measure of energy lowering due to charge transfer. The electrophilicity index is defined as follows:

$$\omega = \left(\frac{\mu^2}{2\eta}\right)$$

This parameter permits the classification of organic molecules as strong, $\omega > 1.5$ eV, moderate, $0.8 < \omega < 1.5$ eV, and marginal electrophiles, $\omega < 0.8$ eV. On the other hand, a good correlation between the inverse of the electrophilicity (ω) can be made, thus molecules located at the bottom of the electrophilicity scale classified as marginal electrophiles corresponds as good nucleophiles [30]. However, when the molecule bears more than one functional group with opposite electrical charge, its nucleophilic character cannot be straightforwardly associated with the inverse of the electrophilicity. Thus the nucleophilicity index (N) appears as a different descriptor which gives more information about nucleophilicity and is defined [31]:

$$N = E_{HOMO} - E_{HOMO(TCE)}$$

where tetracyanoethylene (TCE) is taken as reference. All these properties were calculated using these equations for the indole alkaloids through B3LYP/6-311G (2d,p) basis sets and their values are shown in Table 1.

As seen in Fig. 5 the calculated HOMO and LUMO orbitals comprise the entire structure in both molecules and show similar surfaces forms, however, (**2**) has a HOMO-LUMO gaps slightly smaller than the calculated for structure (**1**) (differentiated by 0.51 eV), indicating structure (**2**) to be more reactive. The hardness values reveal that structure (**2**) is softer than (**1**), showing to be more polarizable with tendency of a charge distribution (presenting values of 1.69 and 1.94 eV respectively). Structure (**1**) appears to be more electronegative (with $\chi = 3.87$ eV), indicating a significative attractive electron power, while alkaloid **2** reveals to be more nucleophilic since the electrons are further from the nucleus due to the more polarizability (with $\chi = 3.78$ eV). In fact the addition of a hydroxil group at position 9 reduced the HOMO-LUMO gap indicating that the presence of substituents in the indole moiety influences the reactive properties, which can reflect in their pharmacological properties (see sections 3.6 and 3.7). Comparing these hardness values with the calculated for other know alkaloids like liriodenine ($\eta = 1.81$) [32], strychnobrasiline ($\eta = 2.66$), 12-hidroxy-10, 11-dimethoxystrychnobrasiline ($\eta = 2.51$) [33] and 9-methoxycanthin-6-one ($\eta = 1.94$) [34], the alkaloids (**1**) and (**2**) present values that classifies them as soft molecules.

3.4. IR analysis

A total of 87 and 90 normal vibration modes were obtained for structures **1** and **2** respectively, but only modes between 400 and 4000 cm^{-1} were compared with the experimental spectrum. Figs. 6 and 7 show the experimental and theoretical IR spectra comparison. The differences around can be attributed to the fact that the theoretical DFT calculations were made for the molecules in the gas phase, whereas intermolecular interactions occur experimentally. The assignment of the experimental bands to the normal modes of vibration was made by the calculated potential energy distribution (PED) using the optimized structures with the lowest potential energy at B3LYP/6-311G (2d,p) calculation level (see Tables 2 and 3). In order to investigate the performance of the calculated theoretical wavenumbers, the root mean square deviation (RMSD) values between the theoretical scaled (scale factor of 0.9802) and the observed wavenumbers were calculated.

Table 1
Calculated energy values for annomontine (1) and *N*-hidroxyannomontine (2) using B3LYP/6-311G (2d, p) basis sets.

Parameters	1	2
Energy (a.u.)	−852.253067	−927.43589
E_{HOMO} (eV)	−5.81453	- 5.47683
E_{LUMO} (eV)	- 1.92819	- 2.09582
$E_{HOMO-LUMO}$ (eV)	3.88634	3.38101
Hardness (η)	1.94317	1.69051
Chemical potential (μ)	−3.87136	−3.78633
Electronegativity (χ)	3.87136	3.78633
Electrophilicity index (ω)	3.85643	4.24022
Nucleophilicity index (*N*)	4.27810	4.53128

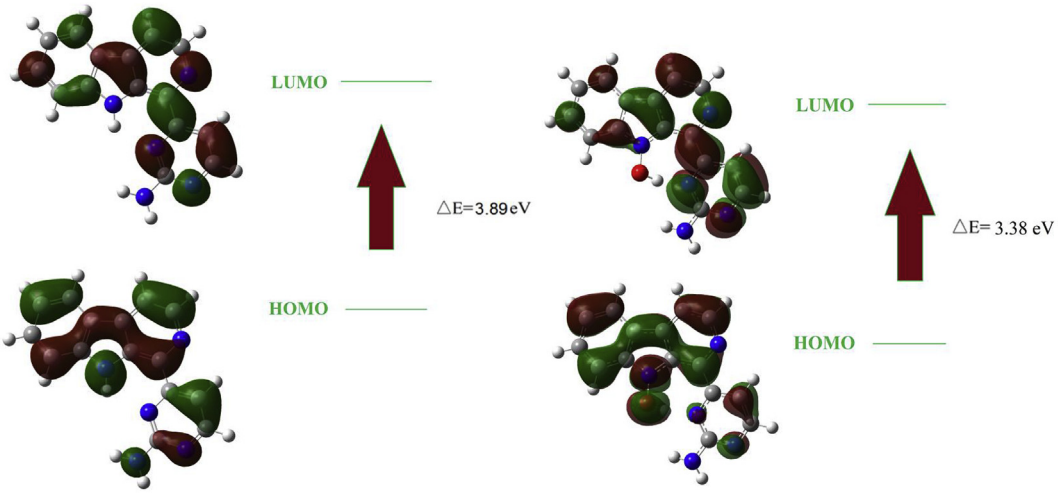

Fig. 5. Frontier molecular orbitals of structures (**1**) and (**2**).

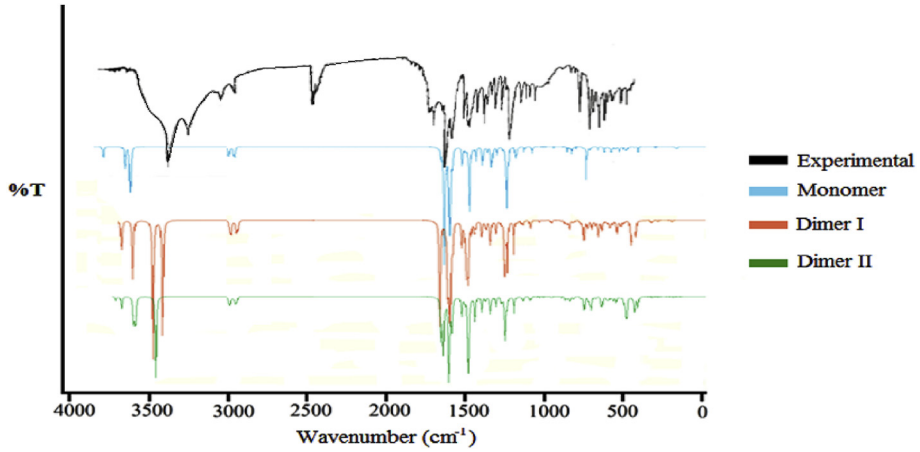

Fig. 6. Comparison between experimental and calculated spectra of Annomontine (**1**).

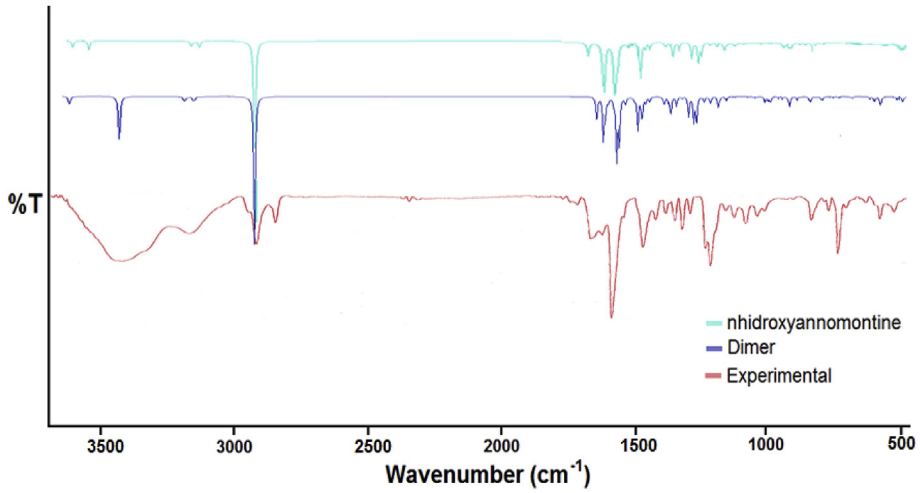

Fig. 7. Comparison between experimental and calculated spectra of *N*-hydroxynnomontine (**2**).

The assignment of the experimental bands of structure **1** (Table 2) shows that the wavenumbers between 3500 and 2800 cm^{-1} are related to N–H stretchings (bands at 3480 and 3346 cm^{-1}) and H–C stretching modes (bands at 3169, 2923 and 2853 cm^{-1}) principally of the A and D ring. Bands between 1700 and 1000 cm^{-1} were related to C=C stretching vibration modes

Table 2
Experimental and calculated wavenumbers (cm^{-1}) and assignments for structure **1**.

IR Solid	B3LYP 6–311 (2d,p)						PED>5%
	Monomer		Dimer I		Dimer II		
	Wavenumber	IR Intensity	Wavenumber	IR Intensity	Wavenumber	IR Intensity	
3480	3526.37	186.68	3529.45	184.73	3506.83	211.85	Stre N9–H9 (99%)
3346	3511.55	46.19	3347.68	619.02	3381.92	614.16	Stre Sym. H–N7′–H (100%)
3169	3172.31	1.99	3172.32	1.38	3181.35	14.16	Stre C5′-H5’ (99%)
2923	3087.32	24.77	3086.81	26.30	3097.19	8.19	Stre C3–H3 (92%)
2853	3081.68	35.65	3076.95	45.32	3077.06	47.72	Stre C6′-H6′ (99%)
1652	1625.82	34.80	1625.27	26.77	1625.50	22.29	Stre C6=C5 (13%) + Stre C7=C8 (13%) + Stre C5–C5a (12%) + Stre C8–C8a (17%) + Bend C5a = C8a-N9 (10%)
1630	1607.87	346.44	1599.96	25.51	1596.13	33.36	Stre N7′-C2′ (10%) + Bend H–N7′-C2’ (48%)
1576	1577.83	365.10	1578.59	213.81	1575.48	283.87	Stre C5′-C6’ (26%) + Stre N1′-C2’ (10%)
1551	1556.18	82.38	1551.39	137.71	1556.3	66.30	Stre N1′-C2’ (12%) + Stre N3′-C1′ (12%)
1467	1476.73	21.38	1479.11	17.48	1478.96	4.18	Bend H3–C3=N2 (20%)
1457	1456.22	22.63	1455.57	39.96	1456.72	56.65	Stre C5a = C8a (10%) + Bend H5–C5=C6 (18%) + Bend H8–C8=C7 (19%)
1419	1414.18	77.89	1417.44	56.32	1414.23	178.81	Stre N3′-C1’ (10%) + Stre N1–C1a (10%) +Bend C1a = C1–N2 (10%) + Bend H4–C4–C3 (14%)
1384	1373.05	64.85	1372.35	71.29	1371.38	75.32	Stre N1–C8a (17%) + Bend H9–N9–C1a (15%) + Bend H7–C7=C8 (13%)
1324	1323.74	7.49	1324.14	10.13	1324.56	14.03	Bend H6–C6–C7 (14%) + Bend H5–C5=C6 (12%)
1288	1284.93	31.05	1284.78	46.79	1286.28	36.00	Stre N2–C1 (13%) + Bend H5–C5=C6 (10%)
1225	1226.73	191.39	1227.71	169.94	1227.38	171.44	Stre N1’ = C6’ (23%) + Stre N3′-C1’ (20%) + Stre N3’ = C2’ (10%)
1175	1172.18	40.26	1172.96	62.19	1171.56	53.84	Bend H9–N9–C1a (20%)
1145	1154.22	5.76	1154.27	6.27	1154.18	4.82	Bend H6–C6–C7 (22%) + Bend H7–C7=C8 (21%) + Bend H8–C8=C7 (12%)
1071	1070.46	18.93	1070.33	23.09	1071.47	18.07	Stre C4–C3 (27%) + Bend H4–C4–C3 (36%)
942	943.01	0.0355	943.38	0.066	945.73	0.0977	Tors H4–C4–C3=N2 (22%) + Tors H3–C3=N2–C1 (52%)
818	828.03	23.07	827.99	23.93	826.96	26.28	Tors H8–C8=C7–C6 (10%) + Tors H4–C4–C3=N2 (37%) +Tors H3–C3=N2–C1 (20%)
740	738.22	64.98	738.79	79.29	739.28	77.05	Tors H6–C6–C7=C8 (30%) + Tors H7–C7–C6=C5 (23%) + Tors H5–C5=C6–C7 (11%) + Tors H8–C8=C7–C6 (12%) + Out C8–N9–C5a = C8a (11%)
701	707.98	2.37	709.95	9.66	709.69	4.65	OUT N7′-C2-N1′-N3’- (21%) + OUT C1–C5′-N3′-C4’ (24%)
668	668.51	7.49	667.64	8.94	666.30	4.44	Bend C5a = C8a-N9 (10%) + Bend C2′-N1’ = C6’ (15%)+Bend C2′-N1’ = C6’ (11%)
630	629.98	28.97	629.99	39.67	632.70	54.01	Bend C7=C8–C8a (16%) + Bend C3=N2–C1 (11%) + Bend C5–C5a = C8a (15%)
616	615.98	6.60	615.55	0.78	616.04	1.62	Tors H9–N9–C1a-C4a (20%) + Tors H3–C3=N2–C1 (10%) + Out C8a-N9-C1a-C4a (17%)
565	560.89	13.18	560.63	9.59	560.96	9.26	Stre C5–C5a (11%) + Bend C5a = C8a-N9 (19%) + Bend C3=N2–C1 (10%)

(assigned to the experimental bands at 1652, 1576, 1457 and 1071 cm^{-1} that corresponds to the calculated scaled wavenumbers 1625, 1577, 1456 and 1070 cm^{-1}), N–C stretching modes (assigned to the experimental bands at 1630, 1551, 1419, 1384, 1288 and 1225 cm^{-1} that correspond to the calculated scaled wavenumbers 1607, 1556, 1414, 1373, 1284 and 1226 cm^{-1}), H–C=N and H–N=C bend vibration modes (1630, 1467 and 1175 cm^{-1} that correspond to the calculated scaled wavenumbers 1476 and 1172 cm^{-1}) and H–C=C bend vibration modes (experimental bands at 1457, 1419, 1384, 1324, 1288 and 1145 cm^{-1}). Bands between 1000 and 400 cm^{-1} are mostly related to torsions (distortions between dihedral angles) of HCCN, HCNC and HCCC type, out of plane torsions of CNCC and NCNN type and bend vibrations mode of NCC, CNC and CCC type. No significant differences were observed between wavelengths values calculated the monomer and for the dimers **I** and **II** (Table 2). However, the values assigned to the stretching of N–H groups of the dimers shows to be closer to the experimental in relation to the monomer, with wavelengths at 3526.3 and 3511.5 cm^{-1} for the monomer, 3529.4 and 3347.6 cm^{-1} for dimer **I** and 3506.8 and 3381.9 cm^{-1} for dimer **II**, while in the experimental spectrum the bands are at 3480 and 3346 cm^{-1}. This implies that the intermolecular interactions involving the NH_2 groups are plausible and directly influenced the infrared spectrum by decreasing the frequency oscillator related to N–H bonds stretchings, causing a reduction in the wavelength (see Fig. 6).

The assignment of the experimental bands of structure **2** (Table 3) shows that the wavenumbers between 3500 and 2800 cm^{-1} are related to N–H stretching modes (broad band between 3500 and 3400 cm^{-1}) H–C stretching modes (bands at 3172 and 2921 cm^{-1}, assigned to C5′-H5′and C6–H6 stretching vibrations) and OH stretching vibration (band at 2852 cm^{-1}). Bands between 1700 and 100 cm^{-1} were related to C=C stretching vibrations (assigned to the experimental bands at 1606, 1574, 1414, 1288 and 1080 cm^{-1} that correspond to the calculated scaled wavenumbers 1617, 1575, 1382, 1286 and 1084 cm^{-1}), C=N stretching vibrations (assigned to the experimental bands at 1465, 1420, 1382, 1228 and 1209 cm^{-1} that correspond to the scaled theoretical wavenumbers 1461, 1432, 1414, 1231 and 1202 cm^{-1}), H–C=C bending vibrations (bands at 1465, 1288, 1209, 1155 and 1123 cm^{-1} that correspond to the calculated scaled wavenumbers 1461, 1286, 1202, 1151 and 1126 cm^{-1}), H–C=N bending vibrations (assigned to the experimental bands at 1465, 1420, 1382, 1317 and 1123 cm^{-1}), H–O–N bend vibration (assigned to the experimental bands at 1664 and 1574 cm^{-1} that corresponds to the theoretical scaled wavenumber at 1663 and 1576 cm^{-1}) and C–C–C bend vibration modes (band at 1038 cm^{-1} that corresponds to the theoretical scaled wavenumber 1044 cm^{-1}). The large differences from 3200 to 4000 cm^{-1} between the experimental data and the theoretical wavenumbers calculated for the monomer (see Fig. 7) are related to the H7′-N7′ stretching, which are indicative that intermolecular interactions by N–H···N hydrogen bonds occur, forming dimers like Fig. 4. The optimized geometry of the proposed N-hidroxiannomontine dimer, stabilized by N7′-H7’—N1'intermolecular hydrogen bonds, showed N–H stretching values (3380 cm^{-1}) closer to the experimental ones (3420 cm^{-1}), implying that the proposed dimer is plausible.

3.5. NBO analysis

NBO analysis describes the Lewis-like molecular bonding pattern of electron pairs (or of individual electrons in the open-shell case) in optimally compact form. NBOs determine the

Table 3
Experimental and calculated wavenumbers (cm^{-1}) and assignments for structure 2.

Experimental	B3LYP 6-311G (2d,p)				PED>5%
	Monomer		Dimer		
	Wavenumber	Ir Intensity	Wavenumber	Ir Intensity	
3420	3515.26	65.95	3380.66	683.37	Stre symm. H–N7′–H (100%)
3172	3181.04	2.17	3184.07	2.94	Stre C5′-H5′ (99%)
2921	3085.81	29.65	3082.22	28.53	Stre C6′-H6′ (99%)
2852	2850.44	1116.31	2812.32	2079.61	Stre O10–H10 (100%)
1664	1663.29	87.35	1673.09	271.38	Bend H10–O10–N9 (75%)
1606	1617.38	94.22	1617.42	22.61	Stre C7=C8 (15%) + Stre C5=C5a (13%)+ Stre C8=C8a (12%)
1574	1575.63	129.69	1576.14	642.25	Stre C5′ = C6′ (12%) + Stre C8a = C5a (12%)+ Bend H–O10–N9 (10%) + Stre C7=C6 (10%)
1465	1461.49	82.81	1472.35	30.83	Bend H6′-C6′-N1′ (10%)+ Stre N9=C8a (10%) + Bend H5′-C5′ = C6′ (10%) + Bend H8–C8–C7 (10%) + Bend H5–C5=C5a (10%)
1420	1432.65	42.76	1435.54	61.36	Stre N9=C1a (11%) + Bend H3–C3=N2 (12%)
1382	1413.72	43.09	1416.46	4.25	Stre N9–C1a (11%)+ Stre C1a = C4a (10%)+ Bend H3–C3=N2 (15%)
1346	1345.66	16.84	1345.75	19.29	Stre C6=C5 (12%) + Stre C7=C8 (10%) + Bend H4–C4–C3 (17%)
1317	1312.86	100.86	1313.54	57.16	Bend H6′-C6′ = N1′ (17%)
1288	1286.18	44.14	1286.35	69.06	Stre C4a = C4 (10%)+ Bend H5–C5=C5a (20%)+ Ring B breathing
1228	1231.38	112.59	1227.95	43.31	Stre N1′ = C6′ (24%)+ Stre N3′ = C4′ (23%) + Stre N3′ = C2′ (11%) + Rocking H–N7′–H (12%)
1209	1202.57	150.75	1202.87	38.81	Stre N1=C2 (19%) + Bend H5–C5=C5a (20%)+ H8–C8=C8a (18%)
1155	1151.41	88.77	1151.45	49.02	Bend H6–C6=C7 (24%) + Bend H7–C7=C6 (20%)
1123	1125.94	4.71	1125.68	15.57	Stre C5′ = C6′ (12%)+ Bend H7′-N7′-C2′ (16%)+ Bend H5′-C5′ = C6′ (52%)
1080	1084.02	49.81	1084.23	108.16	Stre C4=C3 (20%)+ Stre O10–N9 (10%) + Bend H4–C4=C3 (25%)
1038	1043.93	22.25	1044.51	32.22	Ring C breathing + Ring B breathing + Stre N9–O10 (15%)+ Bend C8=C7=C6 (11%)+ Bend C6=C5=C5a (10%) + Bend H5′-C5′ = C6′ (12%)
836	839.34	23.35	839.78	18.92	Tors H10–O10–N9–C8a (59%) + Tors H3–C3–N2–C1 (24%)
772	774.46	7.86	774.32	10.01	Stre O10–N9 (11%) + Bend C4–C3–N2 (23%)
733	737.92	61.35	737.95	55.208	Tors H6–C6–C7=C8 (31%) + Tors H7–C7–C6=C5 (21%) + Tors H5–C5=C6–C7 (16%) + Out C8–N9–C5a-C8a (15%)
634	634.35	14.54	634.20	26.73	Bend C7=C8–C8a (17%) + Bend C5–C5a-C8a (17%)
580	579.09	20.07	579.23	30.55	Stre O10–N9 (10%) + Bend C3–N2–C1 (18%) + Bend N9–C1a-C4a (21%)
529	525.96	3.81	526.39	5.54	Tors C4a = C4–C3–N2 (18%)
440	444.73	8.24	443.14	4.34	Tors H6′-C6′-N1′-C2′ (12%) + Tors C5′ = C6′-N1′-C2′ (29%) + Out C1′-C5′-N3′-C4′ (10%)
402	408.64	217.82	347.65	8.02	Wagg. H7′-N7′-H7′ (85%)

localized *Natural Lewis Structure* (NLS) representation of the wave function, while the remaining "non-Lewis"-type NBOs complete the span of the basis and describe the residual "delocalization effects" by the second-order perturbation energies E (2) [donor (i) → acceptor (j)] that involve the most important delocalization and are given by [35–38]:

$$E(2) = \Delta_{ij} = q_i \frac{F_{ij^2}}{\varepsilon_j - \varepsilon_i}$$

Thus, NBOs provide a valence bond-type description of the wave function, closely linked to classical Lewis structure concepts and is a helpful tool for understanding the delocalization of electron density [37,39–41]. The NBO analysis of molecules **1** and **2** revealed strong hyperconjugative intramolecular interactions of π→π*, LP→π* and LP→σ* type, which are formed by orbital overlaps between C=C bondings and C=C anti-bondings and between N/O lone pairs (LP) and *C*–C/C=C anti-bondings, leading to an intramolecular electronic density transfer causing stabilization of the molecular system in both structures (see Table S2 and S3). For the title structures, the second-order perturbation energies values analysis shows, more precisely, that the greater conjugations values are the π→ π* (C=C→ C=C) hyperconjugations of the indole portion (including the A, B and C Rings), the LP→π* hyperconjugations (N9→ C5a-C8a, N2→C1a-C1 and N7'→N3′-C2′) and the π→ π* type (C=C → C=N) hiperconjugations of the D ring. The σ→σ* type hyperconjugative intramolecular interactions contributes to the stabilization of the systems too, deserving prominence the interactions C6–C5→C5–C4a (5.16 kcal/mol), C7–C8→C8a-N9 (6.03 kcal/mol) and C4a-C1a→C5–C5a (5.33 kcal/mol) for annomontine **(1),** and C5a-C8a→C4a-C4 (5.44 kcal/mol), C5a-C8a→N9–O10 (5.42 kcal/mol) and C6–C5→C5a-C4a (5.25 kcal/mol) for *N*-hydroxyannomontine **(2).**

Concerning to the conformational analysis presented in section 3.1, the conformers 1A and 2A presented hyperconjugative intermolecular interactions of LP→σ* type, which were formed by the electron donation of the N3′ lone pair to H9–N9 σ* bond orbital in 1A (3.87 kcal/mol) and by electron donation of N3′ lone pair to H10–O10 σ* bond orbital in 2A (59.9 kcal/mol), thus justifying the hydrogen bonds which promotes stability for these conformers. The stability of the proposed annomontine (**1**) dimers (see Fig. 4) is theoretically based on the hyperconjugative interactions N1'→H7′ (1.62 kcal/mol) and N3'→H7′ (1.45 kcal/mol) for dimer **I** and N2→H–N7' (6.53 kcal/mol) for dimer **II**. For the proposed *N*-hydroxyannomontine dimer, its stability is theoretically based on the hyperconjugative interactions N1'→H7′-N7' (1.03 kcal/mol for both hydrogen bonds).

3.6. UV–vis analysis

The electronic spectra of the substances were recorded in methanol solution and were compared to the calculated spectra at time dependent density functional theory (TD-DFT) using the B3LYP/6-311G (2d,p) basis set in methanol (PCM model) as showed in Fig. 8. The experimental spectrum of alkaloid **1** showed bands at 222, 291, 300 and 391 nm that were assigned to the sum of the n→π* and π→π* transitions characteristic of β -carboline alkaloids. The theoretical spectrum presented an intense electronic transition of 5.33 eV (with oscillator strength f = 0.6611) at 232.4 nm with major contributions from H→L+3 (75.4%) being equivalent to the experimental band at 222 nm. The calculations also predicted intense electronic transitions at 291.6 nm (with

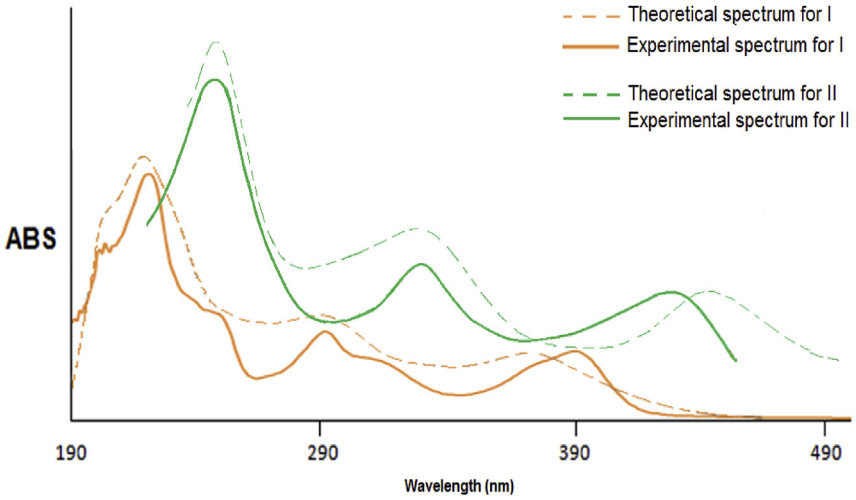

Fig. 8. Comparison between experimental and theoretical UV spectra at B3LYP 6-311G (2d, p) in methanol of annomontine (**I**) and *N*-hidroxyannomontine (**II**).

electronic transition of 4.25 eV and oscillator strength f = 4.2515), 313.6 nm (with electronic transition of 4.36 eV and f = 0.2151) and 384.6 nm (electronic transition of 3.22 eV and f = 0.3792), that are equivalent to the experimental bands at 291, 300 and 391, with contributions from H→L+1 (80.6%) (291.6 nm), H-2→L (75.6%) (313.6 nm) and H→L (98.6%) (384.6 nm).

The experimental spectrum of alkaloid **2** showed maxima at 246, 312 and 428 nm, characteristic of conjugated aromatic chromophore. Compared to the spectrum of structure 1, a bathochromic shift is revealed, due to the presence of the OH group in position 9 that acts as auxocromic group, justified by the hyperconjugative LP→π* interaction of O10 lone pair with N9–C1a bond, showing a second-order perturbation energy value of 6.91 kcal/mol in NBO calculations (see section 3.4 and table S3). The calculated spectrum predicted intense electronic transitions at 245 nm (with electronic transition of 5.05 eV and oscillator strength f = 0.7056), 314 nm (with electronic transition of 3.93 eV and f = 0.2848), and 444 nm (with electronic transition of 2.78 eV and oscillator strength f = 0.2711), showing good agreement with the experimental UV data (see Fig. 8). In respect to the electronic transitions, the tree maximum calculated absorptions correspond to the major transitions contributions from H→L+3 (47.8%) and H-2→L+1 (33.5%) for 245 nm, H-1→L (56.23%) and H-2→L (25.8%) for 314 nm and H→L (99.08%) for 444 nm.

3.7. Prediction of activity spectra (PASS) and molecular docking studies

PASS (prediction of activity spectra) [42] is an online tool that estimates the pharmacological activities of a molecule based on SAR (structure activity releationship) analysis of a data set containing more than 205000 compounds exhibiting more than 3000 kinds of biological activities. Average accuracy of prediction is about 95% according to leave-one-out cross validation (LOOCV) estimation and the probabilities, Pa (probable activity) and Pi (probable inactivity), are values that vary from 0.000 to 1.000, in general Pa + Pi ≠ 1 since these probabilities are calculated independently [43]. The PASS prediction results for the studied alkaloids are listed in Tables 4 and 5. Among various predicted properties, the following activities deserve attention: kidney function stimulant, diabetic neuropathy treatment, antiepileptic, antiprotozoal, polarization stimulant, rheumatoid arthritis treatment, antiasmatic and antineoplastic.

Table 4
Pass prediction for the activity spectrum for annomontine with Pa>0.3.

Pa	Pi	Activity name
0.750	0.009	Kinase inhibitor
0.695	0.008	Protein kinase inhibitor
0.701	0.035	Glycosylphosphatidylinositol phosphalipase D inhibitor
0.665	0.016	Thioredoxin inhibitor
0.667	0.026	Pseudolysin inhibitor
0.668	0.044	Nicotinic alpha6beta3beta4alpha5 receptor antagonist
0.641	0.026	Phtalate 4,5-dioxygenase inhibitor
0.650	0.037	Nicotinic alpha2beta2 receptor antagonist
0.606	0.016	Urethanase inhibitor
0.512	0.089	Kidney function stimulant
0.433	0.020	Diabetic neuropathy treatment
0.465	0.055	Glucose oxidase inhibitor
0.446	0.036	Signal transduction pathways inhibitor
0.420	0.053	Antiepileptic
0.455	0.053	Alkane 1-monooxygenase inhibitor
0.444	0.043	CYP2F1 substrate
0.415	0.014	Cyclopentanone monooxygenase inhibitor
0.413	0.013	Pseudouridylate synthase inhibitor
0.405	0.005	MAP kinase inhibitor
0.477	0.079	Antineoplastic
0.426	0.035	CDK9/cyclin T1 inhibitor
0.420	0.020	Carbon-monoxide dehydrogenase inhibitor
0.408	0.030	Antineoplastic (colorectal cancer)
0.432	0.051	Nucleotide metabolism regulator
0.397	0.020	Antineoplastic (colon cancer)
0.392	0.015	Indolepyruvate *C*-methyltransferase inhibitor
0.407	0.033	DNA-(apurinic or apyrimidinic site) lyase inhibitor
0.396	0.027	Meprin B inhibitor
0.418	0.050	Hydroxylamine oxidase inhibitor
0.436	0.049	CYP2A8 substrate

From this premise, molecular docking calculations were performed on AutoDock-Vina [44] with DNA Topoisomerase II-DNA complex (topo II-DNA) due to the fact that a wide variety of molecules used for the treatment of human cancers (antineoplastics) such as lung, ovarian, brain, breast, adrenocortical and testicular cancers are eukaryotic topo II-DNA inhibitors. The docking calculation in AutoDock Vina (ADTV) consists in a number of sequential steps. Each step involves a random perturbation of the conformation followed by a local optimization (using the Broyden-Fletcher-Goldfarb-Shanno algorithm [42] which is an efficient quasi-Newton method) and a selection in which the step is accepted or not. Each local optimization involves many “evaluations” of the scoring function and the number of evaluations in a local

Table 5
Pass prediction for the activity spectrum for *N*-hydroxyannomonitine with Pa>0.3.

Pa	Pi	Activity name
0.870	0.001	Polarization stimulant
0.662	0.019	Nitrate reductase (cytochrome) inhibitor
0.636	0.005	Rheumatoid arthritis treatment
0.650	0.043	Taurine dehydrogenase inhibitor
0.640	0.033	Pseudolysin inhibitor
0.643	0.051	Glycosylphosphatidylinositol phosphalipase D inhibitor
0.600	0.013	Autoimmune disorders treatment
0.592	0.039	Phtalate 4,5-dioxygenase inhibitor
0.573	0.051	Antineoplastic
0.524	0.002	Iron antagonist
0.586	0.096	Membrane permeability inhibitor
0.509	0.026	Antiasthmatic
0.483	0.011	Antiprotozoal
0.524	0.053	Carboxypeptidase Taq inhibitor
0.524	0.040	(R)-6-hydroxynicotine oxidade inhibitor
0.536	0.066	Antiseborrheic
0.313	0.040	Ferrodoxin hydrogenase inhibitor
0.301	0.030	Hydroxylamine reductase inhibitor
0.333	0.066	Glutamine-phenylpyruvate transaminase inhibitor
0.352	0.088	Aspartate-phenylpyruvate transaminase inhibitor
0.306	0.042	Gamma-D-glutamyl-meso-diaminopimelate peptidase inhibitor
0.358	0.096	Diabetic neuropathy inhibitor
0.438	0.010	Antineoplastic (melanoma)
0.479	0.045	Fibrolase inhibitor
0.402	0.009	Antineoplastic (cervical cancer)
0.409	0.024	MAP3K5 inhibitor
0.444	0.056	Nicotine dehydrogenase inhibitor
0.388	0.127	Nicotinic alpha2beta2receptor antagonist
0.306	0.045	Wound healing agent
0.368	0.113	2-hydroxyquinoline 8-monooxygenase inhibitor

optimization is guided by convergence [44,45]. X-ray crystal structure of human DNA topoisomerase II beta complexed with DNA and amsacrine (PDB ID: 4G0U) [46] was obtained from the Protein Data Bank web site (http://www.rcsb.org/pdb/). Water and amsacrine molecules were removed, Gasteiger charges were assigned and the macromolecule was saved in PDBQT file format using ADTV. A Grid box size of 20 × 16 × 18 Å was centered at the site of DNA cleavage of topo II–DNA complex. The docking protocol was tested by removing the co-crystallized inhibitor amsacrine from the protein and then docking it at the same site (Fig. 9). The superimposition of the structures showed RMSD = 0.399, RMSD, values up to 2 Å are considered reliable for a docking protocol. For comparison, a docking calculation was also performed with doxorubicin (used for the treatment of breast cancer, bladder cancer, Kaposi's sarcoma, and acute lymphocytic leukemia) for being the standard substance of the cytotoxicity tests in section 3.7 (Fig. 10). Free energy of binding (ΔG) analysis demonstrated that molecules **1** and **2** docked with ΔG values of −10.6 and −11.5 kcal/mol (Fig. 11) respectively, while the know inhibitors amsacrine and doxorubicin docked with free energy values of −10.0 kcal/mol and 9.9 kcal/mol respectively.

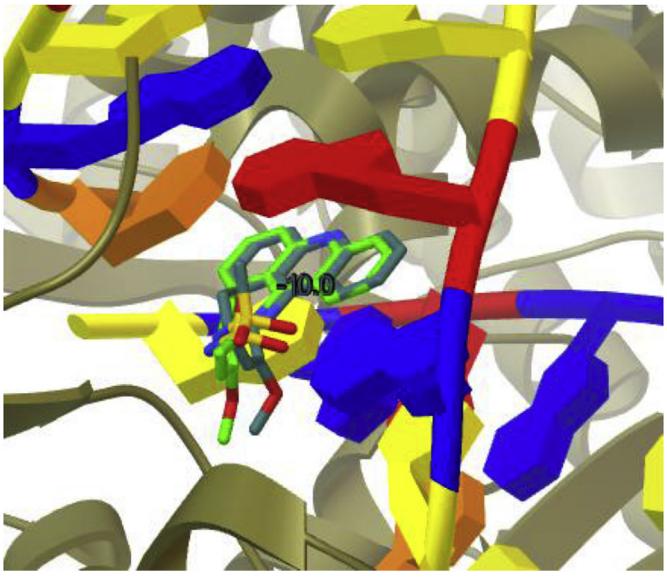

Fig. 9. Superimposition of the docked (dark green) and co-crystallized (green) structure of amsacrine into the DNA cleavage site of DNA topoisomerase II. (For interpretation of the references to color in this figure legend, the reader is referred to the Web version of this article.)

Annomontine (**1**) binds at the catalytic site by weak non-covalent interactions as π− π, π −alkyl and amino-alkyl interactions. Ring A interacts with Glu522 by π −alkyl interaction, B and C Rings interacts with bases Dg13 and Da12 by π- π and π −alkyl interactions, D ring interacts with Arg503 by amino-alkyl interaction and with bases Dc 8 and Dt9 by π- π, π −alkyl and amino-alkyl interactions. *N*-hydroxyannomontine (**2**) binds at the catalytic site by weak non-covalent interactions as π- π and π −alkyl interactions. A ring interacts with bases Dc 8 and Dt9 by π- π, π −alkyl interactions, B, C and D rings interacts with bases Dg13 and Da12 by π- π interactions, NH_2 interacts with Gly504 by amino-alkyl interactions. Both structures bind at the topoisomerase II-DNA complex by π-π interactions between aromatic rings and both upstream and downstream base pairs, interacting similar to amsacrine, revealing a possible anticancer potential for them. However, it's important to note that annomontine has two dimerization forms, while *N*-hydroxyannomontine has only one (see Fig. 4). The spatial arrangement of the annomontine dimers prevents the interaction with topoisomerase II–DNA complex site, while for *N*-hydroxyannomontine the spatial arrangement of its dimer does not appear to prevents such interaction.

3.8. Cytotoxicity assay

The registered IC_{50} values (the half maximal inhibitory concentration) were 17.1, 69.2, 70.6, 90.2 and > 96.2 μM for *N*-hydroxyannomontine and 0.4, 1.5, 1.3, 4.2 and 9.4 μM for doxorubicin in front of HepG2, HL60, K562, B16–F10 and PBMC cells lines respectively. Annomontine (1) did not presented cytotoxicity against the tested cell lines (IC_{50} > 96.7 μM). The antineoplastic potential, registered in the PASS (prediction of activity spectra), and the good affinity with DNA topoisomerase II-DNA complex, suggested by the docking calculations, of *N*-hydroxyannomontine (**2**) alkaloid shown to be plausible in view of the cytotoxicity revealed by this molecule, principally against cell line HepG2 (human hepatocellular carcinoma). For cell line K562 (human chronic myelocytic leukemia) and for PBMC (peripheral blood mononuclear cell - normal lymphoblasts), alkaloid 2 did not revealed cytotoxicity. Annomontine (**1**) did not exhibit significant cytotoxicity against the tested tumor cell lines despite the good prediction in the PASS and the good affinity with DNA topoisomerase II-DNA complex in the docking calculations. The formation of dimers (sections 3.2 and 3.4) may influence the cytotoxic activity of annomontine because prevents the interaction of the molecule with the topoisomerase II-DNA complex and also, the theoretical calculated partition coefficient, using the available on-line software ALOGPS 2.1 program [47], revealed log P values of 1.47 and 2.83 for *N*-hydroxyannomontine and annomontine respectively, showing that *N*-hydroxyannomontine presents a better permeability than annomontine. Doxorubicin presents a theoretical log P value of 1.41.

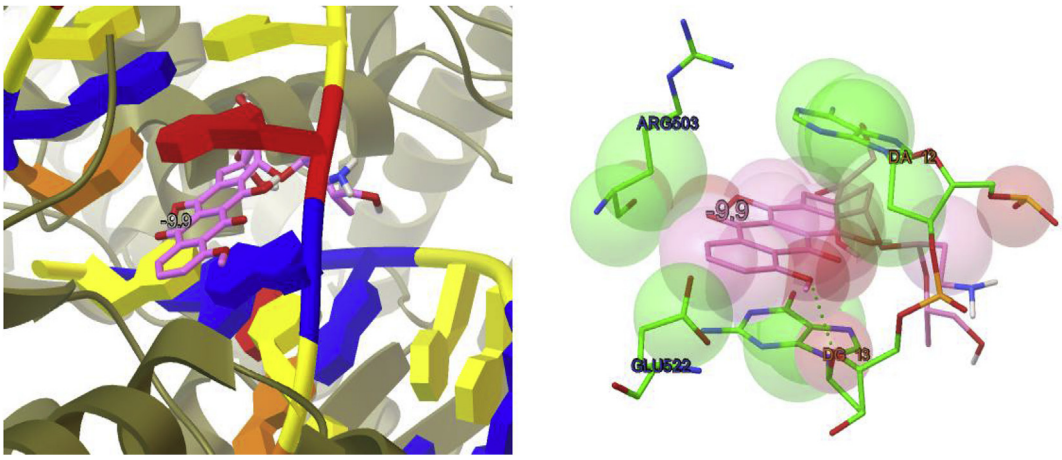

Fig. 10. Interactions of doxorubicin docked to topo II-DNA complex.

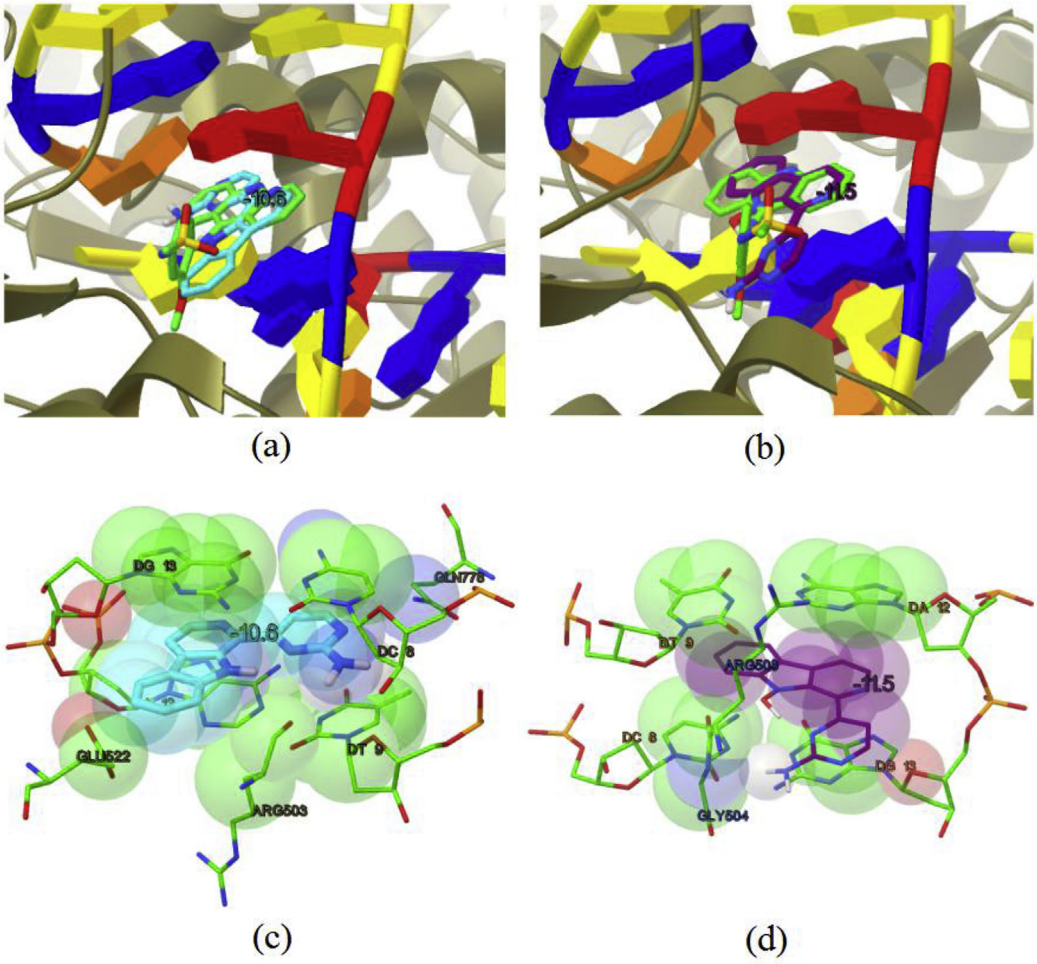

Fig. 11. Binding modes of the studied β-carboline alkaloids docked to Topoisomerase II-DNA complex; (a) Superinposition of the docked annomontine (ciano) and co-crystallized structure of amsacrine (green); (b) Superimposition of the docked *N*-hydroxyannomontine (purple) and co-crystallized structure of amsacrine (green); (c) Annomontine-Topoisomerase II-DNA complex interactions; (d) N-hydroxyannomontine-Topo II-DNA complex interactions. (For interpretation of the references to color in this figure legend, the reader is referred to the Web version of this article.)

4. Conclusion

Annomontine (**1**) and N-hydroxyannomontine (**2**), previously isolated from *Annona foetida,* were comprehensively characterized with their spectral behavior and quantum properties described. The theoretical geometry optimization data compared to the X-ray data of annomontine showed closed values with RMSD values of 0.9158 and 0.9765, for **1** and **2** respectively. The conformational analysis of

both structures revealed that conformations 1A (annomontine) and 2A (*N*-hydroxyannomontine) are the most stable, due to the presence of intramolecular hydrogen bonds (N9–H···N3′ in 1A and O10–H···N3′ in 2A) that gives stability for these conformations. The HOMO-LUMO gap of **2** is slightly smaller than the calculated for **1** (~0.51 eV), revealing **2** slightly more reactive, however, compared to the calculated HOMO-LUMO gap for other alkaloid in the associated literature, annomontine and *N*-hydroxyannomontine can be classified as soft molecules. The hardness values reveal 2 is softer than 1, showing 2 to be more polarizable. Electronegativity (χ) values reveals 1 to be slightly more electronegative than 2, but 2 reveals to be more nucleophilic (Nucleophilicity index) due to the more polarizability. The MEPS calculation leads to infer dimers for both molecules and the comparative IR studies showed that the intermolecular hydrogen bonds, of such dimers, influence the wavenumbers values, making them closest to the experimental ones, implying that structures are plausible. The IR analysis also revealed several characteristic vibrations for both structures that may be used as a diagnostic tool for other β-carboline type alkaloids, simplifying their identification and structural characterization. The electronic spectra of the structures showed consistent with the experimental spectra, with bands assigned to the sum of $n\rightarrow\pi^*$ and $\pi\rightarrow\pi^*$ transitions with bathochromic shift of structure **2** in relation to **1**, justified by the hyperconjugative $LP\rightarrow\pi^*$ interaction of O10 substituent with the five-membered ring (showing an energy value of 6.91 kcal/mol in NBO calculations), acting as an auxocromic group. Molecular docking calculations showed that both structures present a good interaction with DNA-Topoisomerase II complex, with ΔG values of −10.6 and −11.5 kcal/mol for annomontine and *N*-hydroxyannomontine respectively, while the know inhibitors amsacrine and doxorubicin showed $\Delta G = -10.0$ kcal/mol and −9.9 respectively. In vitro Cytotoxicity assay revealed an expressive antitumor activity for *N*-hydroxyannomontine, with emphasis on cytoxicity against human hepatocellular carcinoma cell line HepG2. Annomontine did not show significant cytotoxicity against the tumor cell lines tested, which can be explained by the formation of dimers and by the relatively high value of log P, making this molecule more sensitive to the type of cell membrane protein.

Conflicts of interest

The authors declare that there is no conflict of interests regarding the publication of this paper.

Acknowledgments

The authors thank Capes and Finep for the financial support.

Appendix A. Supplementary data

Supplementary data related to this article can be found at https://doi.org/10.1016/j.molstruc.2018.06.054.

References

[1] A. Dias, A.P. Varela, M. da, G. Miguel, A.L. Macanita, R.S. Becker, J. Phys. Chem. 96 (1992) 10290.
[2] C. Carmona, M. Galan, G. Angulo, M.A. Munoz, P. Guardado, M. Balon, Phys. Chem. Chem. Phys. 2 (2000) 5076.
[3] J.R.F. Allen, B.R. Holmstedt, Phytochemistry 19 (1980) 1573.
[4] A.M. Morin, Brain Res. 321 (1984) 151.
[5] K.P. Lippke, W.G. Schunack, W. Wenning, W.E. Muller, J. Med. Chem. 26 (1983) 49.
[6] T.J. Hagen, P. Skolnick, J.M. Cook, J. Med. Chem. 30 (1987) 750.
[7] J. Ishida, H.K. Wang, K. F.Bastow, C.Q. Hu, K.H. Lee, Bioorg. Med. Chem. Lett 9 (1999) 3319.
[8] J. Jiménez, L. Riverón-Negrete, F. Abdullaev, J. Espinosa-Aguirre, Rodríguez Arnaiz, Exp. Toxicol. Pathol. (60) (2008) 381–389, https://doi.org/10.1016/j.etp.2007.12.003.
[9] R. Stohler, H. Rommelspacher, D. Ladewig, Eur. Psychiatr. 10 (1995) 56.
[10] Z. Xu, F.R. Chang, H.K. Wang, Y. Kashiwada, A. T.McPhail, K.F. Bastow, Y. Tachibana, M. Cosentino, K.H. Lee, J. Nat. Prod. 63 (2000) 1712.
[11] P. Schuup, T. Poehner, R. Edrada, R. Ebel, A. Berg, V. Wray, P. Proksch, J. Nat. Prod. 66 (2003) 272.
[12] A.T. Evans, S.L. Croft, Phytother Res. 1 (1987) 25.
[13] R.B. Pedroso, L.T.D. Tonin, T. Ueda-Nakamura, B.P. Dias Filho, M.H. Sarragiotto, C.V. Nakamura, Ann. Trop. Med. Parasitol. 105 (2011) 549–555.
[14] R. Cao, W. Peng, Z. Wang, A. Xu, Curr. Med. Chem. 14 (2007) 479–500.
[15] M. Leboeuf, A. Cave, A. Forgacs, J. Provost, J. Chem. Soc., Perkin Trans. 1 (1982) 1205.
[16] T.H. Yang, M.Y. Cheng, Taiwan Yaoxue Zazhi 39 (1987) 195.
[17] F. Bracher, D. Hildebrand, Liebigs Ann. Chem. 8 (1993) 837.
[18] K.-S. Chen, F.-R. Chang, Y.-C. Chia, T.-S. Wu, Y.-C. Wu, J. Chin. Chem. Soc. 45 (1998) 103.
[19] E.V. Costa, M.L.B. Pinheiro, C. M Xavier, JRA Silva, A.D.L. Souza, A.C.F. Amaral, A. Barison, F.R. Campos, A.G. Ferreira, G.M.C. Machado, L.L.P. Leon, J. Nat. Prod. 69 (2006) 292.
[20] E.V. Costa, M.L.B. Pinheiro, C.M. Xavier, J.R.A. Silva, A.C.F. Amaral, A.D.L. Souza, A. Barison, F.R. Campos, A.G. Ferreira, G.M.C. Machado, L.L.P. Leon, Magn. Reson. Chem. 46 (2008) 69–74.
[21] M.J. Frisch, G.W. Trucks, H.B. Schlegel, G.E. Scuseria, M.A. Robb, J.R. Cheeseman, G. Scalmani, V. Barone, G.A. Petersson, H. Nakatsuji, X. Li, M. Caricato, A. Marenich, J. Bloino, B.G. Janesko, R. Gomperts, B. Mennucci, H.P. Hratchian, J.V. Ortiz, A.F. Izmaylov, J.L. Sonnenberg, D. Williams-Young, F. Ding, F. Lipparini, F. Egidi, J. Goings, B. Peng, A. Petrone, T. Henderson, D. Ranasinghe, V.G. Zakrzewski, J. Gao, N. Rega, G. Zheng, W. Liang, M. Hada, M. Ehara, K. Toyota, R. Fukuda, J. Hasegawa, M. Ishida, T. Nakajima, Y. Honda, O. Kitao, H. Nakai, T. Vreven, K. Throssell, J.A. Montgomery Jr., J.E. Peralta, F. Ogliaro, M. Bearpark, J.J. Heyd, E. Brothers, K.N. Kudin, V.N. Staroverov, T. Keith, R. Kobayashi, J. Normand, K. Raghavachari, A. Rendell, J.C. Burant, S.S. Iyengar, J. Tomasi, M. Cossi, J.M. Millam, M. Klene, C. Adamo, R. Cammi, J.W. Ochterski, R.L. Martin, K. Morokuma, O. Farkas, J.B. Foresman, D.J. Fox, Gaussian 09, Revision D.01, Gaussian, Inc., Wallingford CT, 2016.
[22] R. Dennington, T. Keith, J. Millam, Gaussian Version 5, Semichem. Inc., Shawnee Missions KS, 2009.
[23] M. Jamroz, Vibrational Energy Distribution Analysis, VEDA 4 Computer Program, Poland, 2004.
[24] J. O'brien, I. Wilson, T. Orton, F. Pognan, Eur. J. Biochem. 267 (2000) 5421–5426.
[25] S.A. Ahmed, R.M. Gogal, J.E. Walsh, J. Immunol. Meth. 170 (1994) 211–224.
[26] Y. Yokomori, K. Sekido, T.-S. Wu, H.-J. Tien, S. Hirokawa, Bull. Chem. Soc. Jpn. 55 (1982) 2236–2238.
[27] R. Parr, G. Pearson, Absolute hardness: companion parameter to absolute electronegativity, J. Am. Chem. Soc. 105 (1983) 7512–7516.
[28] R. Parr, Functional Theory of Atoms and Molecules, Oxford University Press, New York, 1989.
[29] R. Parr, L. Szentpaly, S. Liu, Electrophilicity index, J. Am. Chem. Soc. 121 (1999) 1922–1924.
[30] L.R. Domingo, P. Pérez, The nucleophilicity N index in organic chemistry, Org. Biomol. Chem. 9 (2011) 7168–7175.
[31] L.R. Domingo, E. Chamorro, P. Perez, Understanding the reactivity of captodative ethylenes in polar cyclo addition reactions. A theoretical study, J. Org. Chem. 73 (2008) 4615–4624.
[32] R.A. Costa, P.O. Pitt, M.L.B. Pinheiro, K.M.T. Oliveira, A. Barison, K.S. Salomé, E.V. Costa, Spectrochim. Acta 174 (2017) 94–104.
[33] R.A. Costa, M.L.B. Pinheiro, K.M.T. Oliveira, E.V. Costa, Vibrational, structural and electronic properties investigation by DFT calculations and molecular docking studies with DNA topoisomerase II of strychnobrasiline type alkaloids: a theoretical approach for potentially bioactive molecules, J. Mol. Struct. 1145 (2017) 254–267.
[34] R.A. Costa, M.T. Oliveira, R.C.S. Nunomura, E.A.S. Junior, M.L.B. Pinheiro, E.V. Costa, A. Barison, Quantum chemical properties investigation and molecular docking analysis with DNA topoisomerase II of β-carboline indole alkaloids from Simaba guianensis: a combined experimental and theoretical DFT study, Struct. Chem. (2017). https://doi.org/10.1007/s11224-017-1029-5.
[35] B.C. Carlson, J.M. Keller, Orthogonalization procedures and the localization of wannier functions, Phys. Rev. 105 (1957) 102–103.
[36] F. Weinhold, J.E. Carpenter, J. Mol. Struct. 169 (1988) 41–62.
[37] A.E. Reed, R.B. Weinstock, F. Weinhold, Natural populationanalysis, J. Chem. Phys. (1985) 735–739.
[38] E.R. Davidson, Reduced Density Matrices in Quantum Chemistry, Academic Press, New York, 1976.
[39] R.S. Mulliken, J. Chem. Phys. (1955) 1833–1841.
[40] A.E. Reed, F. Weinhold, J. Chem.l Phys. 78 (1983) 4066–4073.
[41] J.K. Badenhoop, F. Weinhold, J. Chem. Phys. 14 (107) (1997) 5406–5421.
[42] A. Lagunin, A. Stepanchikova, D. Filimonov, V. Poroikov, PASS: prediction of activity spectra for biologically active substances, Bioinformatics 16 (2000) 747–748.
[43] S. Parasuraman, Prediction of activity spectra for substances, J. Pharm. Pharmacol. 2 (2017) 52–53.
[44] O. Trott, A.J. Olson, Software news and update AutoDock Vina: improving the

speed and accuracy of docking with a new scoring function, efficient optimization and multithreading, J. Comput. Chem. 31 (2010) 455–461.
[45] J. Nocedal, S.J. Wright, Numerical Optimization, Springer Series in Operations Research, Springer Verlag, Berlin, 1999.
[46] C.C. Wu, Y.C. Li, Y.R. Wang, T.K. Li, N.L. Chan, On the structural basis and design guidelines for type II topoisomerase-targeting anticancer drugs, Nucleic Acids Res. 41 (2013) 10630–10640.
[47] I.V. Tetko, V.Y. Tanchuk, J. Chem. Inf. Comput. Sci. 42 (2002) 1136–1145.